S. Afshan, J.B.Y. Yu, J.R. Standing, R.L. Vollum, D.M. Potts (2017) Ultimate capacity of a segmental grey cast iron tunnel lining ring subjected to large deformations. Tunnelling and Underground Space Technology; **64**: 74-84.

Ultimate capacity of a segmental grey cast iron tunnel lining ring subjected to large deformations

S. Afshan [(a)], J.B.Y. Yu [(b)], J.R. Standing [(c)], R.L. Vollum [(c)], D.M. Potts [(c)]

[(a)] Brunel University, London, UK, formerly Imperial College London, UK

[(b)] BuroHappold Engineering, formerly Crossrail Ltd and Imperial College London, UK

[(c)] Imperial College London, UK

Abstract

Understanding the behaviour of existing tunnels subjected to in-service deformations, as a result of the construction of underground works (e.g. new tunnels) in their proximity, is of importance in order to safeguard infrastructure within the urban environment. The associated deformations that take place during tunnelling have to be carefully assessed and their impact on the existing tunnels needs to be considered. A half-scale segmental grey cast iron (GCI) tunnel lining ring was tested as part of an extensive research project investigating the impact of new tunnel excavations on existing tunnels conducted at Imperial College London. A sophisticated experimental arrangement was developed to deform the ring in a variety of modes under combined displacement and load control. This paper reports on experiments carried out to assess its structural response when subjected to large deformations. The tests reported are the first to be conducted on a realistic scale model under carefully controlled conditions, and provide valuable insight into the behaviour of a GCI segmental ring during distortions commonly observed in reality. Details of the experiments, including the adopted test set-up and the instrumentation employed, are presented. The measured bending moments around the ring, as a result of the applied deformations, are determined and compared with those predicted using the well-known equations given by Morgan (1961) and Muir Wood (1975), often used in industry, as well as those obtained assuming an elastic continuous ring.

Keywords: bending moment, experiment, grey cast iron, tunnel lining, ultimate capacity.

1. Introduction

With increasing exploitation of underground space within the urban environment, particularly for transportation infrastructure, there is frequently a need to excavate close to existing tunnels. In London, and other major cities, many of the existing tunnels were constructed

more than a century ago, are lined with grey cast iron segmental linings and form part of dense underground transport systems. The trains that run within them often have a tight kinematic envelope and so minimising deformations from nearby excavations is crucial. It is equally important to understand the stress and bending moment regimes within the tunnels to assess how close they are to yielding or, in the extreme, failure. A comprehensive study by Imperial College London has investigated this complex boundary value problem through three main activities: (i) field monitoring of the ground and existing tunnels during nearby construction of the new Crossrail tunnels; (ii) performing sophisticated structural tests on a half-scale segmental lining and (iii) analysing the ground and structural elements using the Imperial College Finite Element Program (ICFEP). Further details of the research project and a summary of the main findings are given by Standing et al. (2015). This paper describes and presents results from the final stages of the second activity.

2. Experimental investigation

2.1 Overview

Achieving a detailed understanding of the development of stresses, bending moments and bolt forces as a tunnel lining deforms can only be assessed realistically using large-scale models. The philosophy with the test set-up used in the study described here was to use half-scale segments (the smallest size that could be cast such that true proportionality of all dimensions was possible) bolted together to form a ring which was deformed using a combination of load and displacement control by means of actuators rather than soil. Prior to embarking on the half-scale set-up, the methodology was checked using a simplified small-scale model (Standing and Lau, 2017).

In the past, other researchers have used large- or full-scale segments to investigate lining response, usually with particular attention focussed on the behaviour and influence of the joints. In all cases, loads were applied directly (e.g. by pressure membranes, load actuators or tensioned tie rods) rather than via a soil medium. Leung (1967) and Thomas (1977) tested cast iron segments while more recently there have been investigations into concrete segments with traditional steel reinforcement (Mashimo et al., 2001, 2002; Blom, 2003; Bilotta et al., 2006; Okano, 2007; Cao et al., 2008). Full rings were tested in a number of these studies, the largest being the ring of 15 m outer diameter and 2 m width used to analyse the linings for the

Shanghai Yangtze River tunnel (Cao et al., 2008). Such tests have also been performed to assess new materials such as fibre-reinforced concrete (Ahn, 2011; Blazejowski, 2012).

In this study, grey cast iron (GCI) half-scale lining segments were cast using a similar chemical composition to that of Victorian age GCI segments used in the London Underground (LU) network. The geometric details of the original segments were also carefully replicated. The adopted scale was dictated by the limitation of casting the thinnest part of the segments (the web/skin). Two principal test set-ups were developed and utilised in the structures laboratory at Imperial College London. The first was for performing two-segment tests, similar to those of Thomas (1977), with a primary aim of investigating joint behaviour; full details of the tests and their modelling assumptions using numerical analysis are reported by Yu (2014). The second involved a full ring, made up of six half-scale GCI segments bolted together, where two series of tests were performed to assess the ring's response when subjected to: 1) small elastic deformations; and 2) large plastic deformations, representative of the serviceability and ultimate limit states, respectively.

In these tests, the ring was first loaded radially to simulate ground stresses acting on the lining in situ (loads were applied uniformly in this stage). It was then deformed into elliptical shapes of similar form and magnitude to those observed in existing tunnels. A detailed description of the experimental set-up and the instrumentation employed along with the results of tests at small elastic displacement levels are given by Yu (2014) and Yu et al. (2017). This paper reports on the results of the tests on the full ring when it was taken to high strain levels and ultimate failure. Only a summary of key components of the experimental set-up is provided (details can be sourced in Yu, 2014 and Yu et al., 2017). The planning of the tests, the adopted loading procedure and how the bending moment distribution compares with those from prediction methods available are discussed in detail.

2.2 Test set-up and instrumentation

A total of six GCI segments, each with an arc length of approximately 1 m, were bolted together and placed on the floor in the Structures Laboratory, such that the radial plane of the ring was horizontal. The assembled model segmental lining ring had inner and outer diameters of 1.781 m and 1.905 m respectively and was 0.254 m in width. It rested on bearings to minimise friction and was surrounded by a steel reaction ring. Figure 1 shows a schematic diagram of the test set-up used, with the various components annotated. Radial

loading of the ring was achieved through a total of sixteen actuators, located at 20° intervals around the circumference of the ring. Spreader pads were used to distribute the load from the actuators to the extrados of the test segment. The actuators in Figure 1 at 250° and 290° were replaced with reaction rods attached to spreader pads in order to prevent rigid body motion of the ring. Each reaction rod was fitted with a load cell. In addition, a tangential tie was fixed to the ring to further increase the overall stability of the ring against rotation.

Electrical resistance strain gauges were used to measure changes in strain on the surface of the GCI segments as a result of the applied loads and deformations. A combination of T-rosette gauges and uniaxial strain gauges, orientated to measure the circumferential bending strains (the strain component used for determining the bending moments in the segments), were installed on segments H, I and J at 20° and 40°, 100° and 90° and 140° and 160°, respectively, as illustrated in Figure 2. A total of eighteen displacement transducers were used to measure radial displacements of the ring intrados during testing. Each displacement transducer was located radially at the lower circumferential flange and aligned with each actuator location. Load cells fitted to the actuators and to the two reaction rods were used to measure the loads applied to the segments. Linear variable differential transformers (LVDT) were used to measure the opening and closing of the joints at 0°, 60°, 120° and 180°. At each of these joint locations, three LVDTs on the intrados of the longitudinal flange and three corresponding LVDTs on its extrados were installed. The LVDTs were aligned with the upper edge bolt, middle bolt and the outer edge of the upper circumferential flange – see Figure 3.

Mild steel, grade 4.6, 12 mm diameter bolts were used in this research, as it was not practicable to manufacture wrought iron bolts as used in the LU tunnels. The results of tensile tests on wrought iron bolts recovered from the Waterloo and City Line, carried out at Imperial College, confirmed the suitability of using mild steel bolts in the laboratory investigations for this research (Yu et al., 2017). The upper and middle bolts in the joints at 0°, 60°, 120° and 180° were instrumented appropriately to measure the change in bolt force during the tests. The first series of tests performed on the ring (Yu et al, 2017), were carefully controlled to avoid exceeding elastic strains, important from the perspectives of changing the properties of the GCI and also strain gauge interpretation. The maximum diametric distortion imposed on the ring was 0.13%. The second phase of testing was to investigate conditions within the ring as ultimate limit state was approached.

2.3 Planning of tests and loading procedure

2.3.1 GCI ring flexural resistance

As part of planning the loading regime for the testing of the GCI segmented ring to failure, the flexural resistance of the GCI segments and joints were first determined. This section discusses the derivation of the combined bending moment-compressive axial load capacity of the GCI segments, allowing for the nonlinear stress-strain behaviour of the material and its asymmetric response in tension and compression. Note that in the case of a circular tunnel lining, axial compressive load relates to the circumferential load (i.e. hoop force) in the ring. The estimated joint bending moment capacities, in the absence of axial compressive force, determined by Yu et al. (2017), namely 1.12 kNm for positive bending (akin to straightening the segment) and 0.72 kNm for negative bending (akin to increasing the curvature of the segment) were adopted. The strength of the joints is enhanced by the presence of axial compressive load in the bolted segmental ring when loaded radially. In the planning of the full ring laboratory tests, the abovementioned joint capacities were adjusted to make due allowance for the contribution of the axial compressive force as explained in Section 2.3.2.

Interaction diagrams were developed between the compressive axial load and bending resistance for the GCI segments assuming nonlinear material behaviour. The nonlinear response was derived from tensile coupon tests on specimens cast at the same time as the GCI segments reported in Yu et al. (2017) – see Figure 4. The compression strength of grey cast iron is approximately three to four times its tensile strength (Angus, 1976). In the absence of measured compressive stress-strain data, the measured tensile stress-strain data were scaled up by a factor of four in the determination of the flexural resistance of the GCI segments.

When the axial force is zero and the mode of bending is positive, i.e., the segment straightens and the extreme fibre at the tip of the circumferential flange is in tension, the flexural resistance is 4.64 kNm (see Figure 5). For the case of negative bending, where the segment increases in curvature and the extreme fibre of the skin is in tension, the flexural resistance is 12.58 kNm. Increasing the axial load, the flexural resistance increases to a maximum of 12.71 kNm for positive bending and 15.64 kNm for negative bending, marking the limits of flange tensile failure and skin tensile failure, respectively. Increasing the axial load beyond these limit points, the flexural resistance starts to reduce, as the failure is controlled by skin compression failure and flange compression failure for positive bending and negative

bending cases, respectively. The maximum compressive capacity of the segment is limited to 2.075 MN, given as the product of the gross cross-sectional area of the segment and the ultimate compressive strength of the GCI material, taken as 480 N/mm^2. The full bending moment-compressive axial load interaction diagram using the nonlinear tensile and compressive stress-strain material models is depicted in Figure 5. The results of a similar analysis based on a linear elastic material model, used for planning of the small displacement tests described by Yu et al. (2017) are also shown for comparison.

2.3.2 Loading procedure

The loading of the ring was carried out in two stages, namely Stage I and Stage II. The loading regime was the same as adopted in the small deformation tests described by Yu et al. (2017), where tests were carried out under hoop forces corresponding to various overburden depths (2 m, 6 m, 12 m and 24 m) and different bolt forces (5 kN, 7.5 kN and 10 kN), with and without grommets. In Stage I, the test ring was loaded at eighteen locations (although only actively at sixteen) evenly distributed around the ring to bring it under a compressive hoop stress corresponding to the depth under consideration, as shown in Figure 6 (a). In Stage II, the load at the designated axis level (90°) was adjusted to unload the ring (P^-), using displacement control, to increase the ring radius, as shown in Figure 6 (b), i.e. induce a squatting deformation. The displacements were applied in small steps with each unloading test taking about 40 minutes to get to 1.2mm radial movement. During Stage II unloading, load control was used to maintain loads in actuators not on the unloading axis equal to loads at the end of Stage I. Additionally, the load in the actuator midway between the fixed reaction points was maintained at the average of the fixed reactions which were similar.

Owing to the limited number of half-scale GCI segments available (two sets of six segments), the tests to distort the ring to large deformations, as described in this paper, were planned to represent the most relevant and critical cases expected in tunnels affected by nearby excavations. With this in mind, the actuators were each loaded to 40 kN in Stage I, corresponding to an overburden depth of 24 m, representing a typical depth of grey cast iron tunnels in the LU network. This was followed by Stage II, where the ring was unloaded along the axis level until failure was reached in either the joint or the segment. Since excavations adjacent to the existing tunnels would generally cause the existing tunnels to unload, it was considered that the unloading tests would provide more relevant information to typical existing in-situ tunnels. Stage II was achieved by setting the actuator at 90° to displacement

control such that the ring was distorted into an ellipse incrementally. The full ring experiments conducted with various bolt pre-loads (5 kN, 7.5 kN and 10 kN), considered to be roughly representative of bolt pre-load values measured in tunnel ring construction practice, indicated no significant difference in the induced bending moment magnitudes and joint deformation behaviour (Yu et al., 2017). Hence, for this final phase of the overall experimental programme, a constant bolt preload of 7.5 kN, with no grommets, was adopted.

An elastic analysis, based on Castigliano's second theorem (Young and Budynas, 2002), was used to obtain an estimate of the axis level displacement required to cause failure of the ring and is described hereafter. The measured elastic modulus of the GCI segments ranged from 80 GPa to 100 GPa (Yu et al., 2017), and was conservatively taken to be 100 GPa. Comparing the predicted bending moment distribution around the ring with the estimated ultimate capacities of GCI segments and joints, the calculations indicated that an outward diametric distortion of 18.7 mm at axis level (90°) would cause failure at joint locations at 0° and 180°, where the maximum positive bending moments occur. The corresponding predicted bending moment distribution around the ring with the segment and joint capacities is depicted in Figure 7. The estimated joint flexural resistances, in the absence of axial load, are 1.12 kNm and 0.72 kNm for positive bending and negative bending cases respectively. The joint flexural resistance is enhanced by the applied compressive axial force. The estimated associated increase in the flexural resistance of the joint, for positive bending, is 1.76 kNm, given as the product of the hoop compressive force (105.98 kN) and the eccentricity of the extrados from the centroidal axis (16.5mm), resulting in a total positive flexural resistance of 2.87 kNm for the considered loading conditions, which matches the applied bending moment of the joints at 0° and 180° locations, where the ring is predicted to first fail. Note that the above-described analyses were only performed to obtain an estimate of the diametric displacement at failure in the tests.

3. Experimental results and discussions

3.1 Loading sequence

Loading of the GCI ring to failure was conducted in two tests, and is described hereafter.

Test 1: The loads in all sixteen actuators were increased to 40 kN (although not controlled, the loads in two fixed reaction points also increased by the same amount), followed by

unloading of the ring at axis level, by setting the actuator at 90° to displacement control. A total outward diametric displacement of 42.1 mm was reached, before the ring was unloaded completely. The corresponding change in load at axis level, from the initial 40 kN, was 20.7 kN. During unloading (i.e. Stage II) the displacement increments were carefully controlled over a fixed time period, but when the applied displacements doubled those predicted at failure of the ring, the rate of unloading was increased. Despite this, after a fifteen-hour shift, the ring had still not fractured and it was decided to stop the Stage II part of the test and unload the radial loads. The measured load-displacement response is shown in Figure 8, where the change in load corresponding to the applied deformation at axis level during Stage II loading is plotted.

Test 2: Test 2 was not originally planned but was required because failure was not achieved after fifteen hours in Test 1. The aim of this test was to reload the ring back to the condition at the end of Test 1, and continue unloading the ring at axis level until failure was reached. Hence, the ring was loaded to 40 kN at all actuator locations, and then unloaded at axis level. A maximum outward diametric displacement of 35.3 mm was recorded before the ring failed. The corresponding change in load at axis level, from the initial 40 kN, was 19.7 kN. The measured load-displacement response is also shown in Figure 8. In this test, the bolts at 0° and 180° locations were replaced with new instrumented bolts, ensuring premature failure of the joints due to possible yielding of the bolts during Test 1 was avoided. Failure of the ring occurred radially in the upper and lower circumferential flanges of a segment J (in Figure 2) with distinct crack locations at a distance of 20 mm offset from the joint at 180 degrees as predicted in the initial assessment. The observed failure modes are presented in Figure 9. The offset of the failure location coincides with where the maximum tensile stresses were determined from the numerical modelling of the GCI two-segment tests reported by Yu (2014). Figure 10 shows the measured displacement around half the ring for both Test 1 and Test 2, after applying corrections for free-body movements. The change in radius in Figure 10 corresponds to the incremental loading in Stage II alone; the maximum values are 24.95 mm for Test 1 and 19.97 mm for Test 2. The maximum change in load at axis level was very similar in Test 1 and Test 2 where failure occurred. Failure is thought to have occurred at a lower change in radius in Test 2 than reached in Test 1 due to the cumulative effect of damage in the ring adjacent to the joint where failure occurred.

3.2 The measured behaviour at the joints

The joint openings at 0°, 60°, 120° and 180° locations as the load at axis level was reduced in both Test 1 and Test 2 are shown in Figures 11 and 12. The positive bending moment at joints 0° and 180° resulted in opening of the joint at the intrados, while the negative bending moment at 60° and 120° caused joint opening at the extrados. As expected, the joint openings at 0° and 180° are significantly larger than at 60° and 120°, due to the lower joint stiffness under positive bending moment. Comparing the results from Test 1 and Test 2, at all joint locations, the amount of joint opening in Test 2 for a given increase in load at axis level is larger; suggesting that the reduced joint stiffness of the GCI ring resulted from the deformations imposed in Test 1. It can also be observed that in Test 1, the joint at 0° did not open by any measureable amount until the load at axis level reduced by more than 10 kN.

Figure 13 shows the change in the bolt force in the upper edge and middle bolts at the 0° and 180° locations for Test 1, where the opening of the joints on the intrados resulted in an increase in the bolt tensile force. As expected, the increases in bolt force are much higher in the upper edge bolts than in the middle bolts, owing to the largest joint openings occurring at the top of the longitudinal flanges; similar observations were made in two-segment tests (Yu, 2014). In comparison, the bolt preload reduced at the 60° and 120° joints by 0.035-0.080 kN during the Stage II loading. Similar trends are evident from the results for Test 2 presented in Figure 14.

3.3 Measured bending moments

The bending moments induced in the ring as a result of the unloading deformations at the end of Stage II loading were calculated from strain measurements at six locations around the ring for both Test 1 and Test 2. These locations are at 20°, 40°, 90°, 100°, 140° and 160°on the ring as shown in Figure 2. The circumferential strains measured at the strain-gauge locations furthest away from the centroidal axis of the segment cross-section were used in the calculations. The stresses were calculated from the changes in strain between the ends of Stage I and Stage II loading assuming that plane sections remain plane. For Test 1, the tensile stress-strain relationship presented in Figure 4, and its scaled up form for compression (see Section 2.3.1), were used to determine the stress from the measured strains. Finally, stress block calculations were used to estimate the change in bending moment from Stage I to Stage II. The resulting bending moments are shown in Figure 15, which also shows the estimated joint flexural resistances (see Section 2). Bending moment distributions calculated for an

elastic continuous ring, using formulae from Young and Budynas (2002) assuming an elastic modulus of 100 GPa, are also depicted in Figures 15 for reference. The bending moment distribution was obtained by adjusting the out-of-balance load at 90° until the analytical equations gave the same displacement as that measured in the experiment i.e. 24.95 mm radial displacement.

For the case of Test 2, where the ring had undergone some degree of plastic deformation as a result of Test 1 loading, the original tensile stress-strain curve (Figure 4), as used for analysis of Test 1, could no longer be used to determine the bending moments. The maximum measured plastic strains at the end of Test 1 for each strain gauge location were identified and are reported in Table 1. A range of bending moments at each strain gauge location was determined, with a minimum value calculated from using the original tensile stress-strain curve and a maximum value calculated from the stress-strain curve associated with the observed level of maximum plastic strain at that section. A series of modified stress-strain curves associated with the observed plastic strains and with reduced Young's modulus values were constructed from the measured tensile stress-strain response of GCI reported by Yu (2014), and are shown in Figure 16. The modified stress-strain curves (curve 1- curve 5) had the following plastic strains ε_{pl} and corresponding Young's moduli E (expressed as a ratio of the original Young's modulus E_0), respectively:

- Curve 1: ε_{pl} = 0 % and E = E_0 (i.e. original stress-strain curve);
- Curve 2: ε_{pl} = 0.025 % and E = 0.86 E_0;
- Curve 3: ε_{pl} = 0.035 % and E=0.85 E_0;
- Curve 4: ε_{pl} = 0.082 % and E=0.81 E_0;
- Curve 5: ε_{pl} = 0.270 % and E=0.71 E_0.

The original compressive stress-strain curve was used owing to the considerably stiffer stress-strain response of cast iron in compression. The maximum and minimum calculated bending moments are reported in Table 1 and plotted in Figure 17 where the moment range at each location is depicted by the marker height. The bending moment distributions calculated for an elastic continuous ring subjected to the measured radial displacement of 19.97 mm are also depicted in Figure 17 for reference.

3.4. Predictions from Morgan's and Muir Wood's equations

The predicted bending moments at tunnel axis (90°), the crown (0°) and the invert (180°) determined using the equation proposed by Morgan (1961) given in Equation (1), assuming elliptical distortion based on a maximum magnitude of radial displacement, are also shown in Figures 15 and 17. It is common industry practice to use Morgan's equation to calculate the bending moment in the tunnel linings, but with a reduced second moment of area according to Muir Wood (1975), given by Equation (2). A simplified form of the Muir Wood's reduced second moment of area, as adopted in earlier versions of LU standard 1-055 (2007), was employed to calculate the bending moments at these locations; these values are also marked in Figures 15 and 17. In the more recent version of this standard, LU standard 1-055 (2014), there is no reference to Muir Wood (1975) and in fact it is suggested (Section 3.4.3.4) that "it is more efficient to start with a simple stiff ring (cylinder with no joints) and then if the assessment fails consider a flexible (jointed) ring". This advice is consistent with the finding of Yu et al. (2017) that for tests conducted under Stage I loads of 40 kN, which are representative of a typical GCI LU tunnel at 20 m to 30 m depth, strain measurements indicated the bolted segmental ring behaved as a continuous ring under an imposed distortion of up to 0.13%.

Morgan's equation:

$$M = \frac{3\delta EI}{a^2} \qquad \text{Eq. (1)}$$

where,

δ = Maximum radial distortion (taken as test measured values at 90°, 0° and 180° – from Figure 9)

a = Tunnel radius (taken as 936 mm)

E = Lining Young's modulus (taken as 100 GPa)

I = second moment of area of lining cross-section (taken as 1309870 mm^4)

Morgan's equation with reduced stiffness:

$$M = \frac{3\delta EI_e}{a^2} \qquad \text{Eq. (2)}$$

I_e = Effective second moment of area of lining, taken as $I_e = (4/n)^2 I$, where n is the number of segments. Note that in Muir Wood's original formulation for I_e there is also an I_J

term, relating to the second moment of area of the joint, but in industry this is often ignored (e.g. LU standard 1-055 (2007)) .

The experimental measurements indicate that using Morgan's equation to calculate the maximum bending moments at 0°, 90° and 180° locations, over-predicts the bending moment at 0° and 180°, where the joint openings are maximum, while providing a closer estimate at 90°. The opposite observations are made using Morgan's equation with reduced stiffness as proposed by Muir Wood (neglecting the I_J term), where the measured bending moment at 90° is under-estimated and those at 0° and 180° are more closely predicted. This is expected, as Morgan's equation uses the full cross-section flexural rigidity (EI) in its formulation, and is best applied at locations where there is minimal loss of stiffness due to joint opening (i.e. 90°), while Muir Wood's equation employs a reduced flexural rigidity (EI_e), and is therefore best suited at locations of significant joint stiffness with maximum joint openings (i.e. 0° and 180°).

With regard to the results from the elastic continuous ring analyses plotted in Figures 15 and 17, from the measured tensile stress-strain curve of GCI segments – see Figure 4, it may be seen that the material response of GCI starts to deviate from linear elastic behaviour at a limiting strain of approximately 0.02%. From the analysis of the measured strains at 90° location in the ring, where the bending moments are greatest, a maximum extreme fibre tensile strain of 0.02% is reached when the imposed diametric displacement is approximately 4 mm. It is therefore proposed that analysis based on linear elastic material behaviour would only apply to ring diametric deformations of below 4 mm which corresponds to a diametric distortion of 0.22%.

4. Conclusions

The two tests discussed in this paper followed on from an extensive series of tests performed on a half-scale GCI ring loaded so as not to exceed elastic strains. There were two stages to all the tests: first a uniform radial load was applied to the outer boundary of the ring to simulate ground stresses; subsequently the ring was unloaded at axis level, whilst maintaining the radial loads at other positions, so as to deform it elliptically. In the later tests the ring was unloaded well into the plastic range in Test 1 and then unloaded to failure in Test 2. The tests reported here are the first to be conducted on a realistic scale model under carefully

controlled conditions and provide valuable insight into the behaviour of a GCI segmental ring during distortions commonly observed in reality.

Unloading the ring resulted in positive bending moments at the designated crown and invert locations (i.e. a straightening of the ring) and negative the bending moments at axis level (resulting in increased curvature of the ring at this location). At locations where the bending moment was positive the joints opened at the intrados of the lining and conversely where it was negative they opened at the extrados.

Estimates of the deformations that had to be imposed at axis level during unloading to cause failure were made using an elastic analysis (estimated value was 18.7 mm). In Test 1 the ring was subjected to deformations of more than twice this predicted value without failure occurring. It was unloaded prior to any failure (because of shift time constraints). On reloading the ring in Test 2, the overall stress-strain response was observed to be softer. Failure occurred suddenly from cracking within the upper and lower circumferential flanges directly adjacent to the joint at the invert (180°). At failure the outward diametric distortion was 35.3 mm (lower than in Test 1) and the actuator load had reduced from 40 kN to 19.7 kN at axis level.

Strain and joint opening measurements indicate that for the applied Stage I loads of 40 kN, which are representative of a typical GCI LU tunnel at 20 m to 30 m depth, the ring behaved like a continuous elastic ring for diametric distortions of up to 0.22% as suggested by LU standard 1-055 (2014) and found by Yu et al. (2017) for distortions of up to 0.13%. Bending moments around the periphery of the ring were calculated at the end of stage II from strain gauge measurements and also estimated using equations and modifications proposed by Morgan (1961) and Muir Wood (1975). For reference, they were also calculated using elastic solutions for a continuous ring according to Young and Budynas (2002). The measurements at maximum applied distortion in both tests indicate that Morgan's equation provides over-estimates of the bending moment at the designated crown and invert levels where bending moments are positive, while better estimates are obtained at the axis level where the bending moments are negative. The converse is observed with the estimates made using the Muir Wood equation with the LU (2007) modification. The two methods are therefore able to provide reasonable estimates of bending moment near failure depending on whether bending moments are positive (i.e. decreasing curvature) or negative (increasing curvature).

Acknowledgements

The authors would like to thank the EPSRC (Grant number EP/G063486/1), Crossrail Ltd, and Morgan Sindall for funding this research project and the London Underground for providing extensive assistance. In particular, thank you to Mr. Mike Black, Dr. Keith Bowers, Mr. Colin Eddie, Mr. David Harris, Mr. Neil Moss, Dr. Barry New, Mr. Sotiris Psomas, and Mr. Peter Wright. The authors must also thank Imperial College research technicians Mr. Duncan Parker, Mr. Steve Ackerley and Mr. Leslie Clark.

References

Ahn, T. (2011) *Thermal and mechanical studies of thin spray-on liner (TSL) for concrete tunnel linings*. Ph.D Thesis, University of Western Ontario, Canada.

Angus, H. T. (1976). *Cast Iron: Physical and engineering properties*. London: Butterworth and Co. Ltd.

Bilotta, E., Russo, G. and Viggiani, C. (2006) Ground movements and strains in the lining of a tunnel in cohesionless soil. *Proc. Int. Symp. Geotechnical Aspects of Underground Construction in Soft Ground*, Bakker et al (eds). Taylor Francis Group, London. pp. 705-710.

Blazejowski, M. (2012) *Flexural behaviour of steel fibre reinforced concrete tunnel linings*. University of Western Ontario. Electronic thesis and dissertation repository, paper 768.

Blom, C.B.M (2003) *Design philosophy of concrete linings for tunnels in soft ground*. Structural Concrete, Vol. 4, No. 2, pp 89-94.

Cao, W.H., Chen, Z.J. & Yang, Z.H. (2008). Study of full-scale horizontal integral ring test for super-large-diameter tunnel lining structure. *The Shanghai Yangtze River Tunnel – theory, design and construction* (ed. R. Huang). Taylor & Francis Group, London.

Leung, K. (1967) *Bolting stresses in tunnel segments*. MSc thesis. University of Glasgow.

London Underground (2007). *Civil Engineering - Deep Tube Tunnels and Shafts*. S.L.: Standard. A1. Report number: 1-055.

London Underground (2014). *Civil Engineering - Deep Tube Tunnels and Shafts*. S.L.: Standard. A3. Report number: 1-055.

Mashimo, H., Isago, N., Shiroma, H. and Baba, K. (2001) Experimental study on static behaviour of road tunnel lining. *Proc. Modern Tunnelling Science and Technology*, Vol. 1, pp 451-456.

Mashimo, H., Isago, N., Yoshinaga, S., Shiroma, H. and Baba, K. (2002) Experimental investigation on load-carrying capacity of concrete tunnel lining. *Proc. 28th ITA General Assembly and World Tunnel Congress AITES-ITA DOWNUNDER.*

Morgan, H. D. (1961). A contribution to the analysis of stress in a circular tunnel. *Géotechnique*. 11.(1). p. 37-46.

Muir Wood, A. M. (1975). The circular tunnel in elastic ground. *Géotechnique*. 25.(1). p. 115-27.

Okano, N. (2007) Development of a testing machine with a large tunnel lining model. *Railway Technology Avalanche*, No. 19, September, p 2.

Standing, J.R., Potts, D.M., Vollum, R., Burland, J.B., Tsiampousi, A., Afshan, S., Yu, J.B.Y., Wan, M.S.P. & Avgerinos, V. (2015). Investigating the effects of tunnelling on existing tunnels. *Proc. Conf. Underground Design and Construction, Hong Kong*, IOM3, Hong Kong Branch, pp 301 – 312.

Standing, J.R. & Lau, C. (2017). Small-scale model for investigation tunnel lining deformations. *Submitted to Tunnelling and Underground Space Technology (October 2015).*

Thomas, H. S. H. (1977). Measuring structural performance of cast iron tunnel linings in laboratory. *Ground Engineering*. 10.(5). p. 29-36.

Young, W. C. and Budynas, R. G. (2002). *Curved Beams. In: Roark's Formulas for Stress and Strains*. New York: McGraw Hill Companies. Inc. p. 267-380.

Yu, J. (2014). *Assessing ground interaction effects and potential damage on existing tunnels before and after new excavation works*. Ph.D. Thesis: Imperial College London. UK.

Yu, J., Standing, J., Vollum, R., Potts, D. and Burland, J. (2017). Experimental investigations of bolted segmental grey cast iron lining behaviour. *Tunnelling and Underground Space Technology*. Vol. 61, pp. 161-178.

List of Tables

Table 1: Measured maximum plastic deformations and bending moments at the end of Test 1

Location in ring	$\varepsilon_{pl,max}$ (%)	Measured bending moment	
		σ-ε curve	M (kNm)
Segment H - 20°	0.025	Curve 1	2.325
		Curve 2	2.514
Segment H - 40°	0.001	Curve 1	0.392
Segment I - 90°	0.270	Curve 1	-9.546
		Curve 5	-9.606
Segment I - 100°	0.082	Curve 1	-6.074
		Curve 4	-6.138
Segment J - 140°	0.005	Curve 1	0.678
Segment J - 160°	0.035	Curve 1	2.979
		Curve 3	3.128

List of Figures

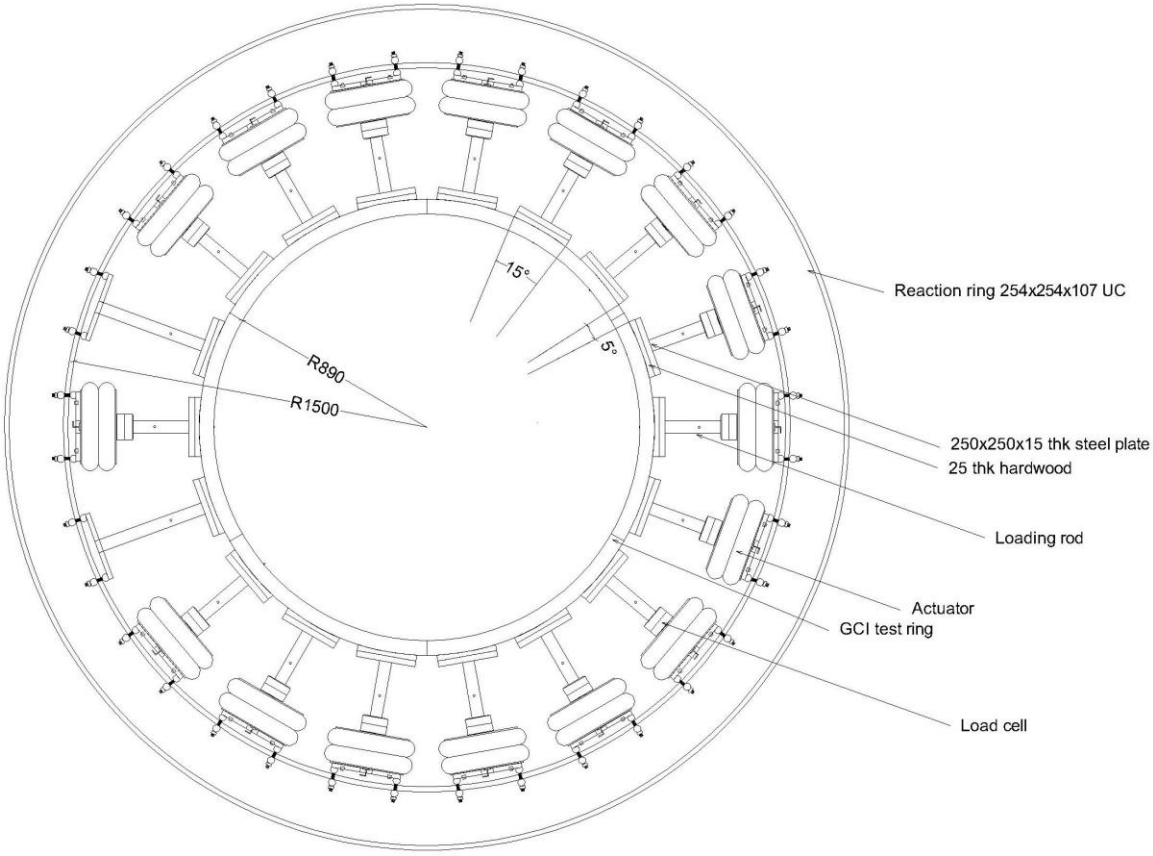

Figure 1: Schematic drawing of the test set-up.

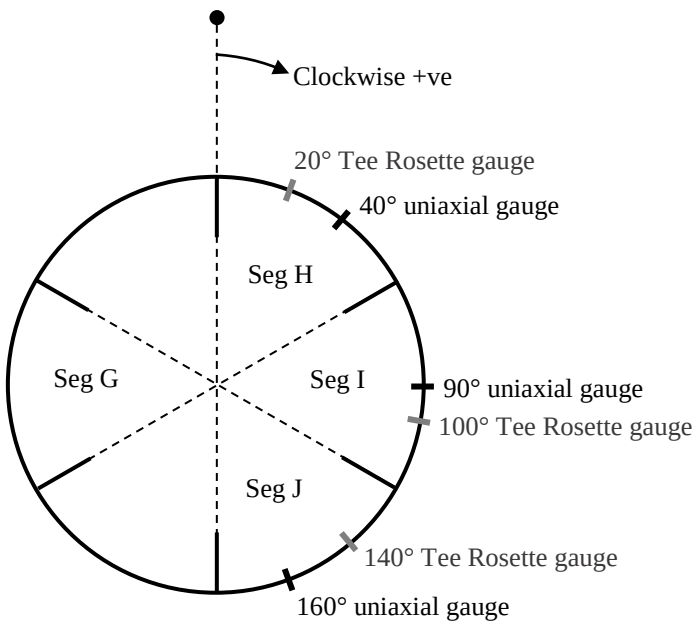

Figure 2: Locations of Tee Rosette and uniaxial strain gauges around the ring.

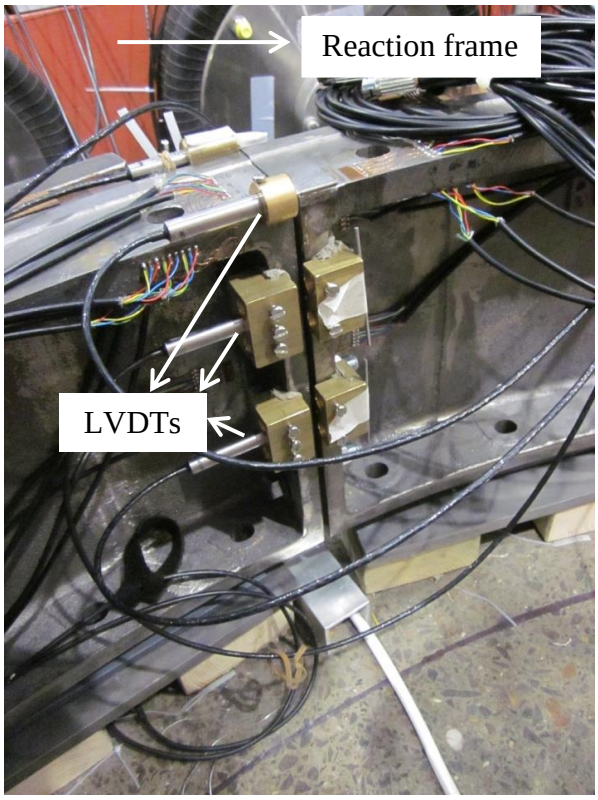

(a) LVDTs on intrados

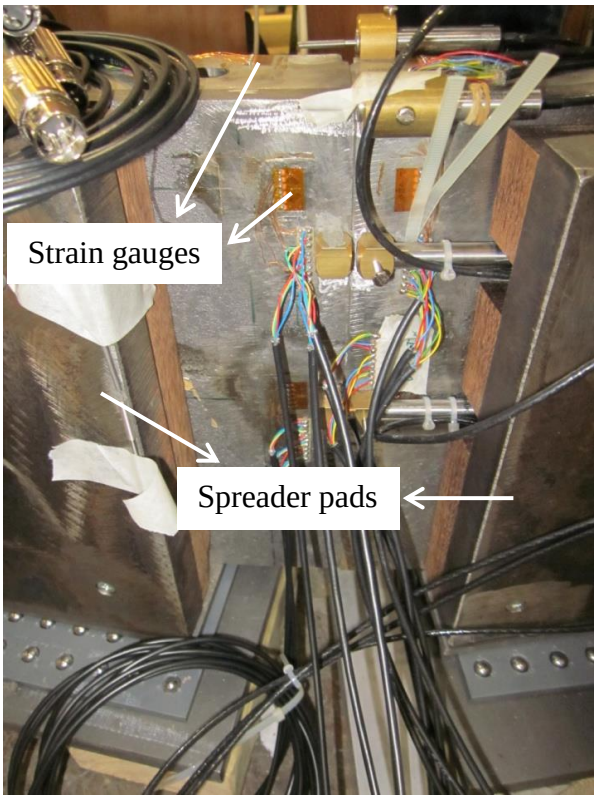

(b) LVDTs on extrados

Figure 3: Locations of LVDTs.

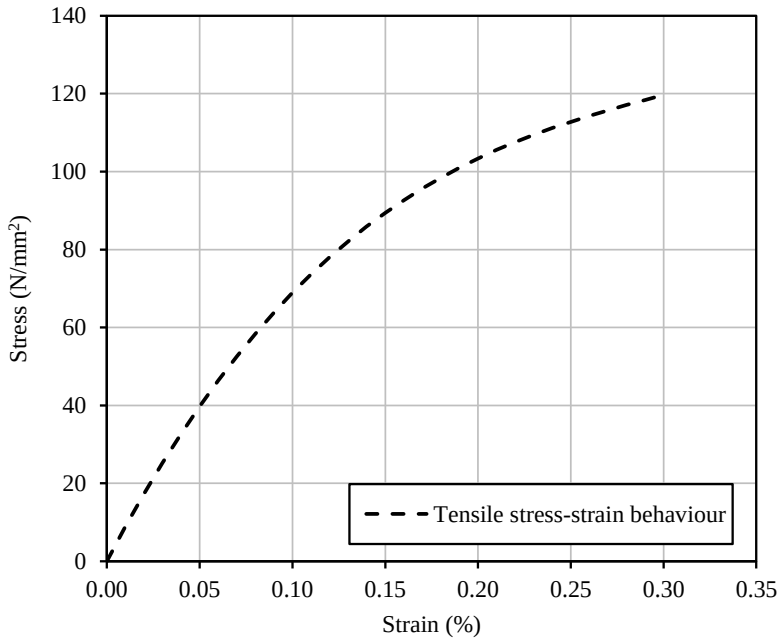

Figure 4: Measured tensile stress-strain behaviour of GCI segment based on coupon tests.

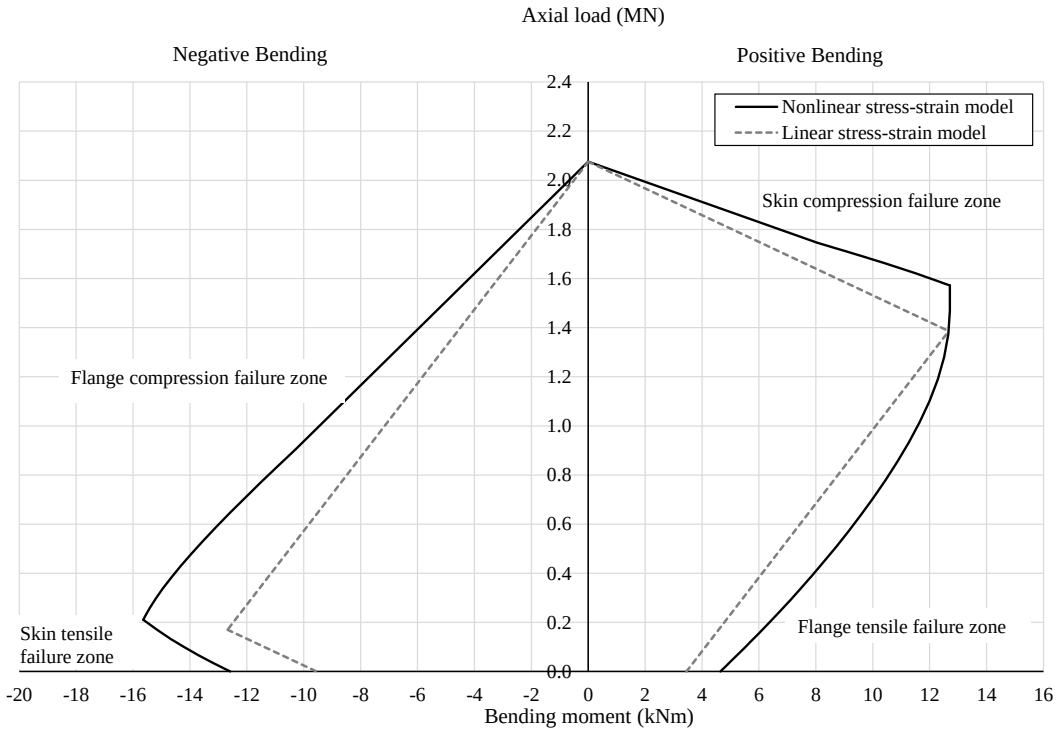

Figure 5: GCI segment combined axial load bending moment capacity.

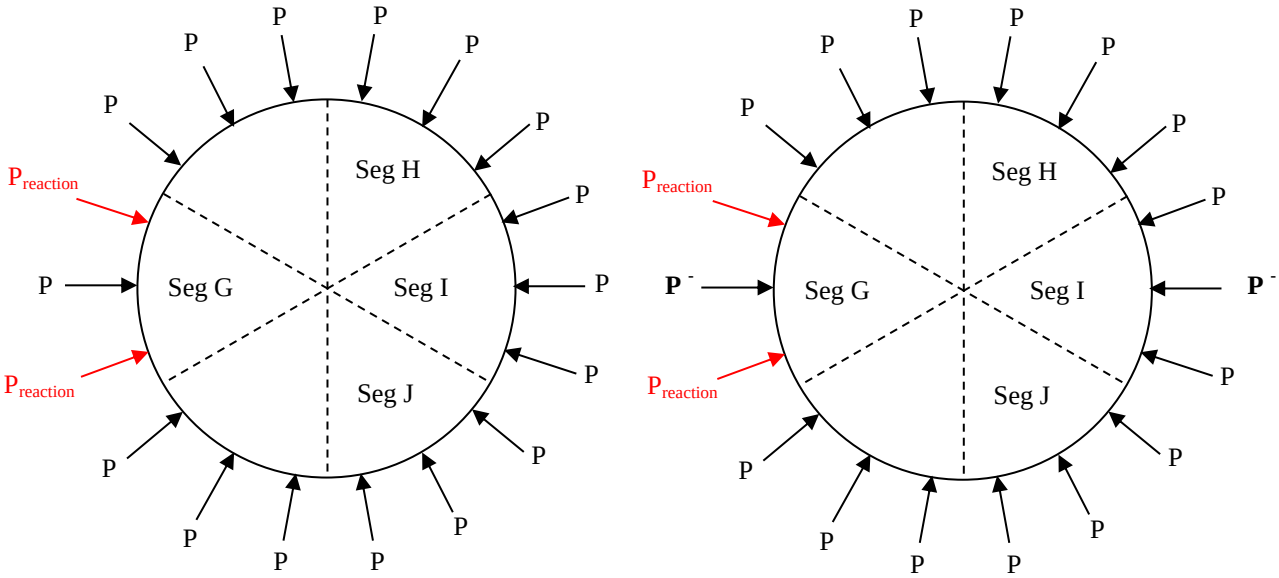

(a) Stage I loading

(b) Stage II loading

Figure 6: Schematic illustration of the ring loading regime for laboratory tests.

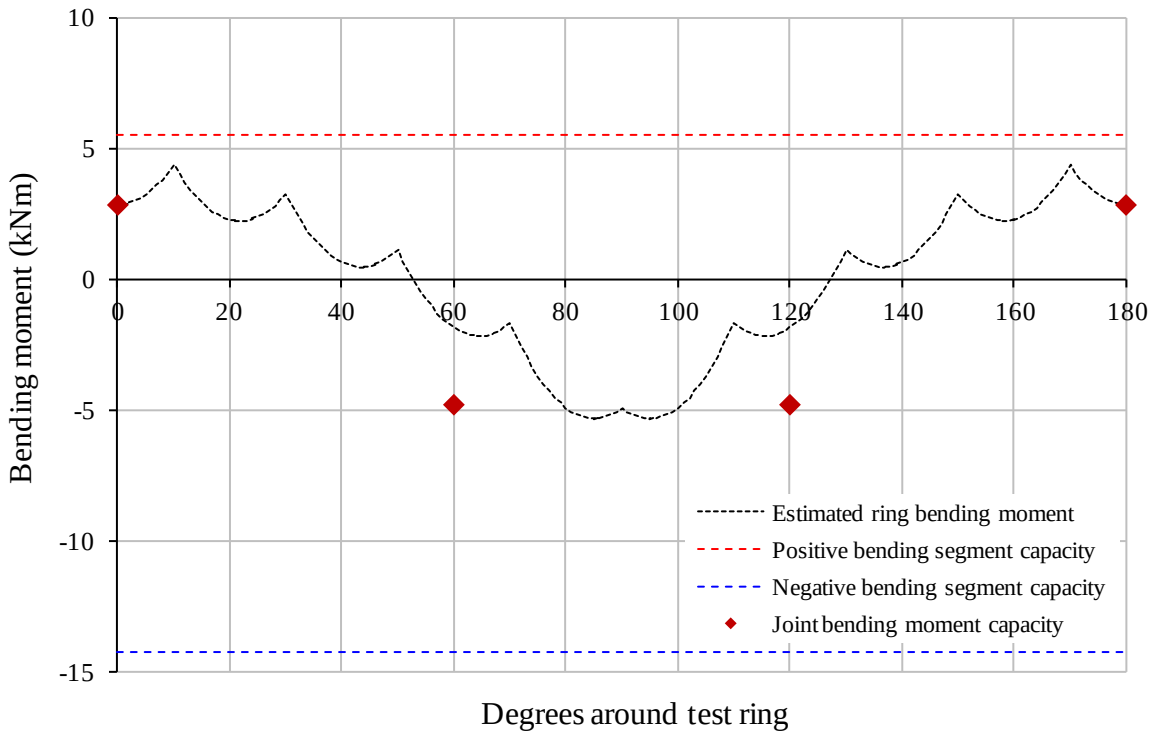

Figure 7: Calculated total bending moment distribution due to 40 kN radial loads and 18.7 mm diametric unloading.

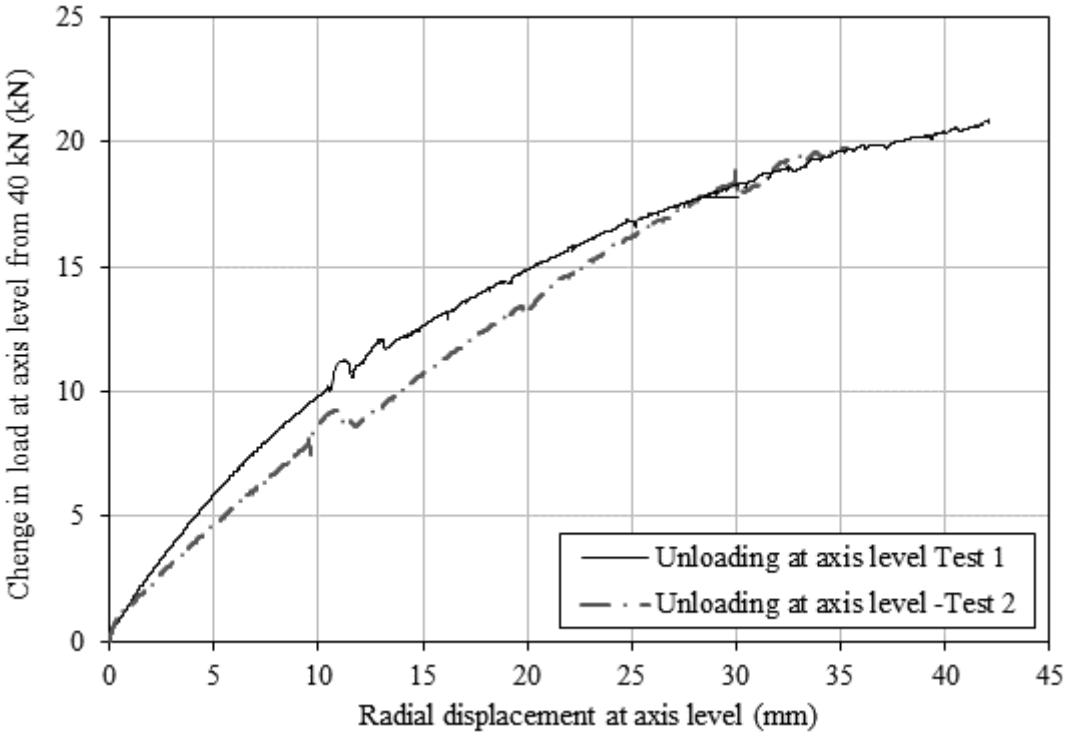

Figure 8: Load-displacement response at axis level for Test 1 and Test 2.

(a) Upper and lower circumferential flange fracture in segment J

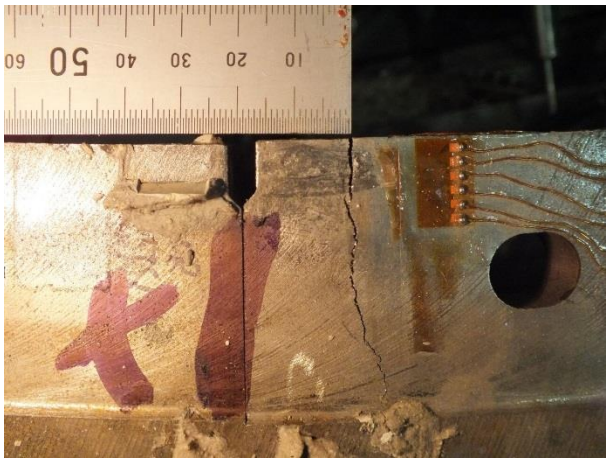

(b) Upper circumferential flange (plan view)

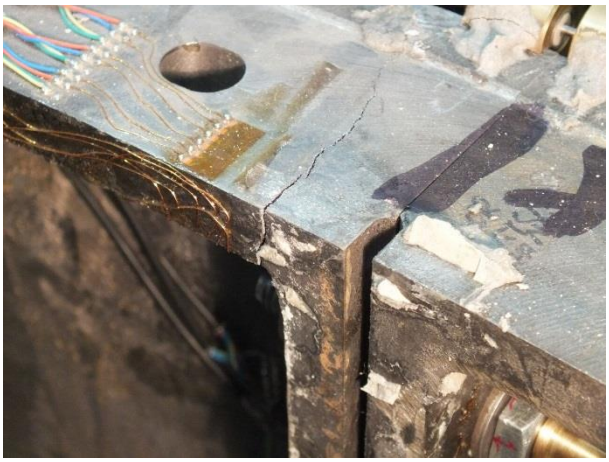

(c) Lower circumferential flange (side view)

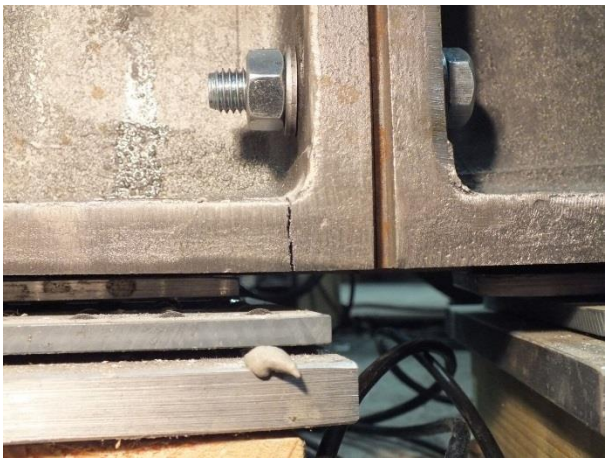

(d) Lower circumferential flange (side view)

Figure 9: Ring failure mode.

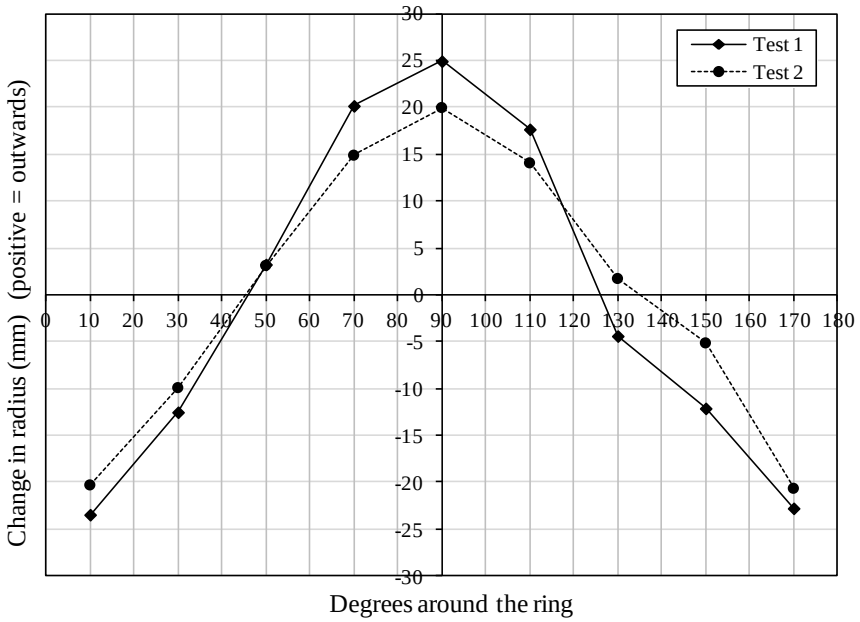

Figure 10: Measured radial displacement for Test 1 and Test 2 during Stage II loading.

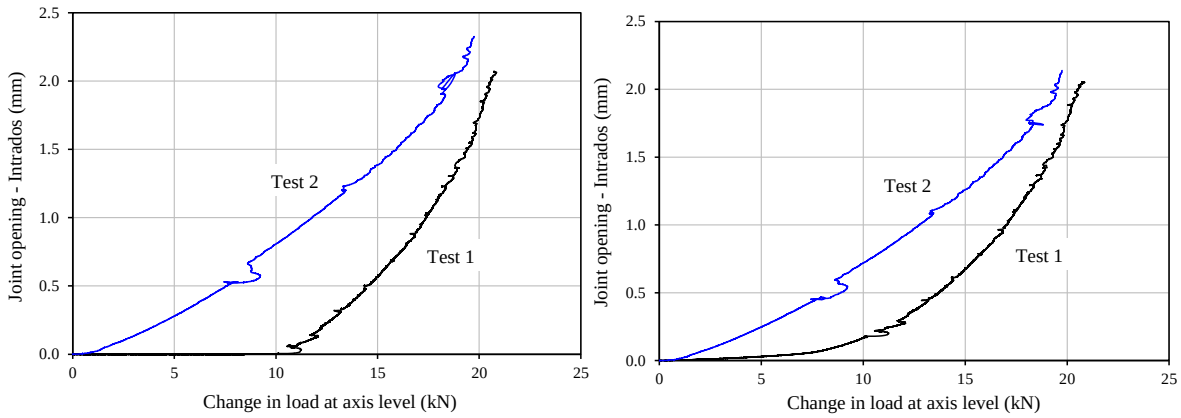

(a) Joint at 0 degrees location (b) Joint at 180 degrees location

Figure 11: Measured intrados joint opening at 0° and 180° locations during Stage II loading.

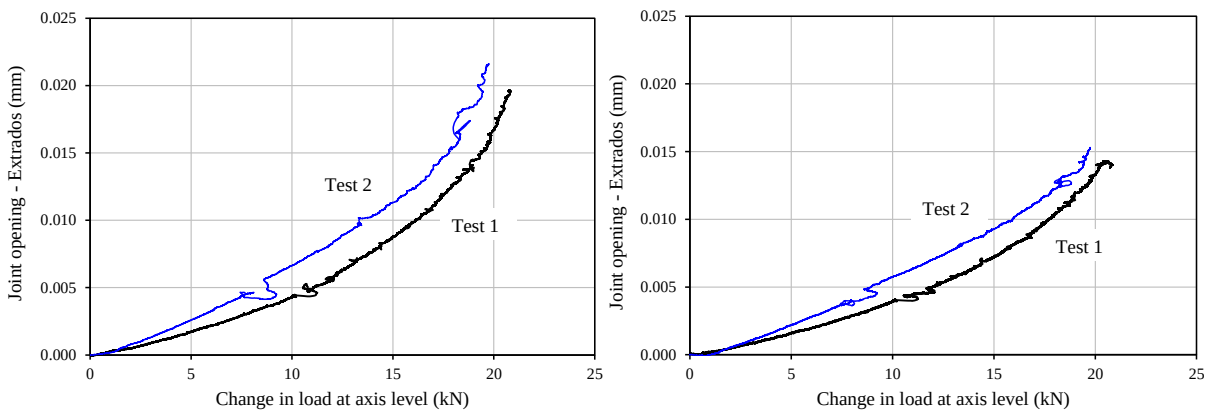

(a) Joint at 60 degrees location

(b) Joint at 120 degrees location

Figure 12: Measured extrados joint opening at 60° and 120° locations during Stage II loading.

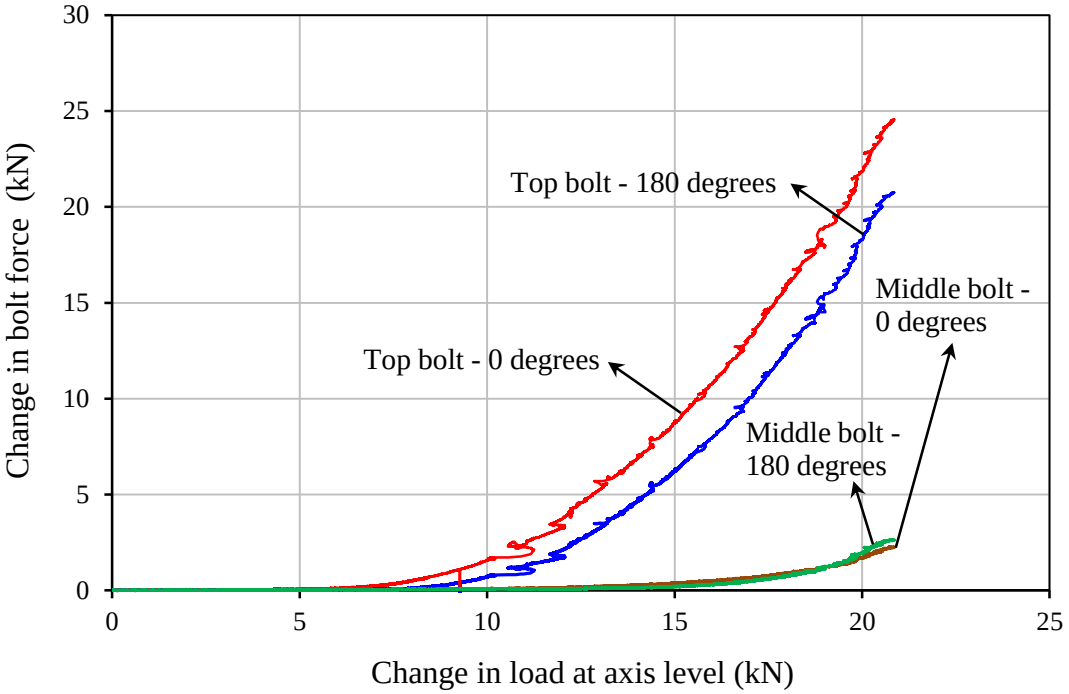

Figure 13: Change in bolt force at 0° and 180° joints during Stage II loading in Test 1.

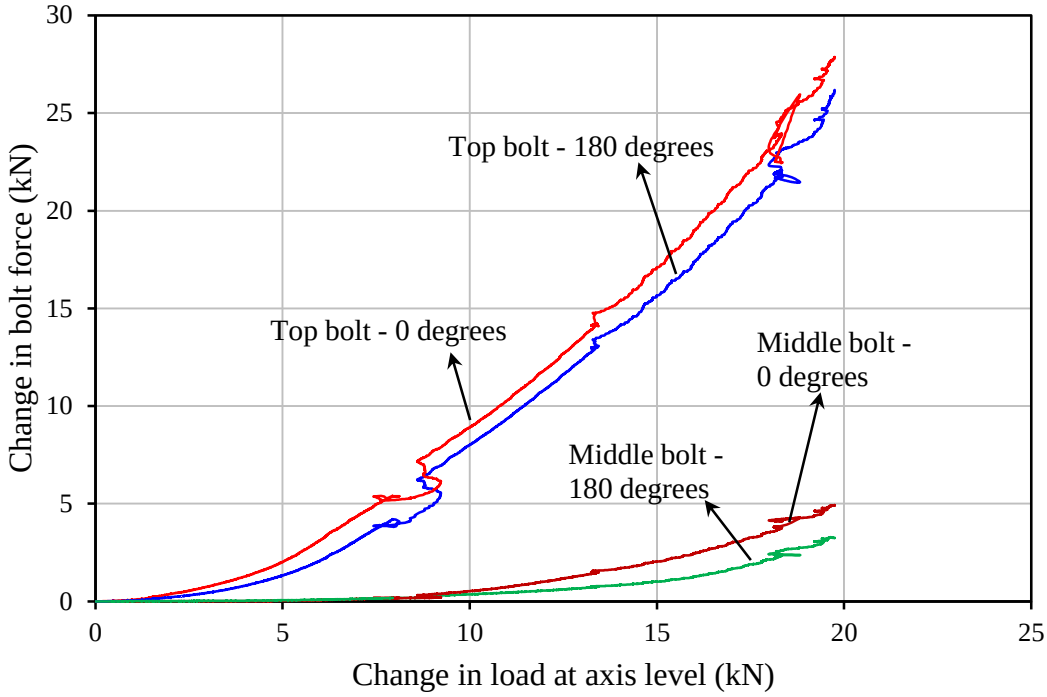

Figure 14: Change in bolt force at 0° and 180° joints during Stage II loading in Test 2.

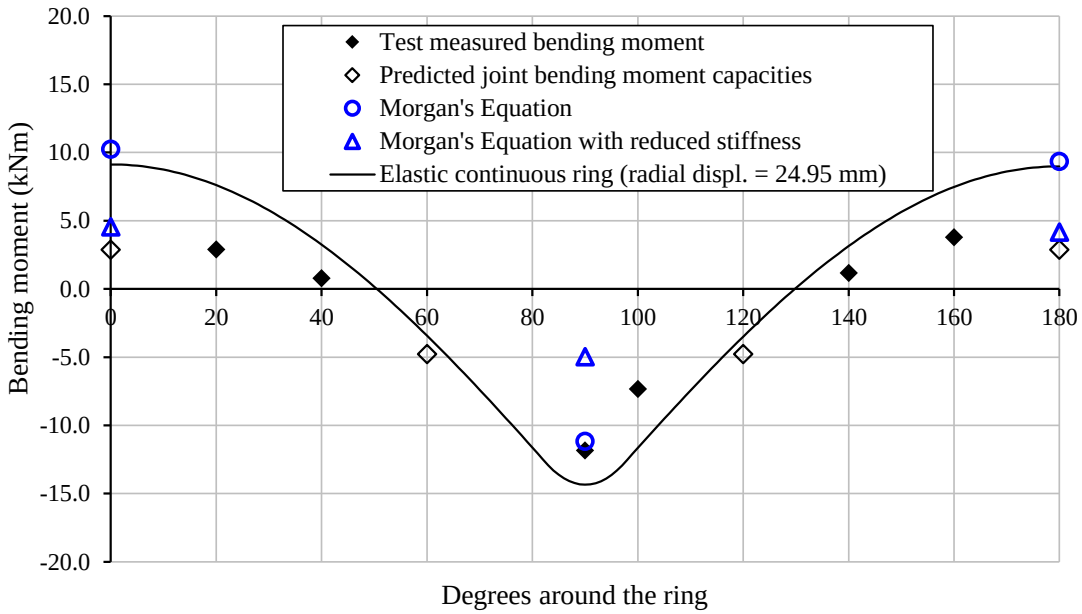

Figure 15: Test measured bending moment distribution around the GCI ring - Test 1.

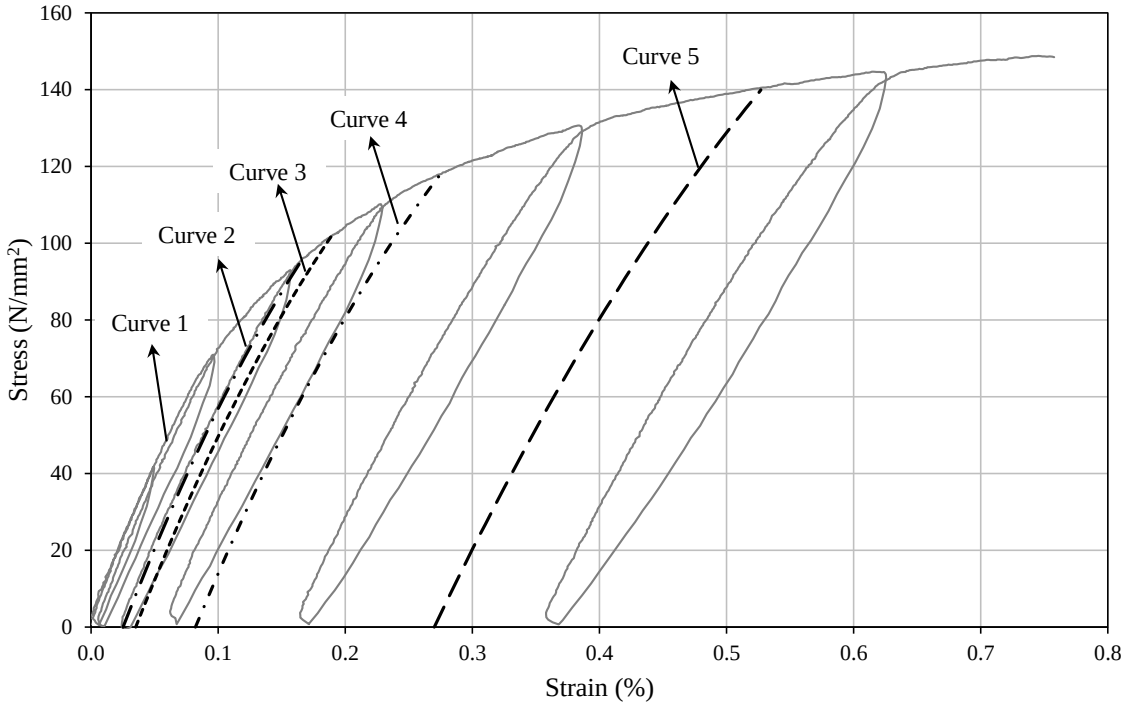

Figure 16: Tensile stress-strain response of GCI with varying levels of permanent plastic strains.

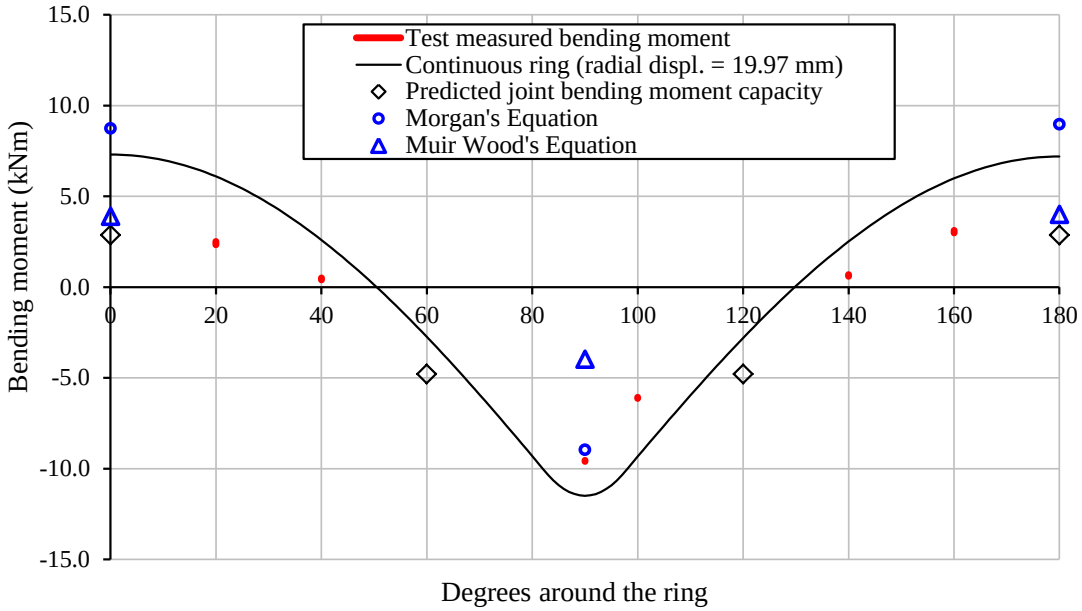

Figure 17: Test measured bending moment distribution around the GCI ring - Test 2.